



CHORUS

This is the accepted manuscript made available via CHORUS. The article has been published as:

Rayleigh-Taylor-instability experiments with elastic-plastic materials

Rinosh Polavarapu, Pamela Roach, and Arindam Banerjee

Phys. Rev. E **99**, 053104 — Published 8 May 2019

DOI: [10.1103/PhysRevE.99.053104](https://doi.org/10.1103/PhysRevE.99.053104)

Rayleigh-Taylor Instability Experiments with Elastic-Plastic Materials

Rinosh Polavarapu^{1*}, Pamela Roach^{2*} & Arindam Banerjee¹

(*Both authors have contributed equally to the work)

¹Department of Mechanical Engineering & Mechanics
Lehigh University, Bethlehem, PA 18015

²Department of Mechanical & Aerospace Engineering
Missouri University of Science & Technology
Rolla, MO 65401

Submitted to : Physical Review E
Original Paper Type : Regular Article
Date Submitted : February 4, 2019
Reviews Received : March 18, 2019
Revision Submitted : April 4, 2019

2nd Reviews Received : April 15, 2019
Revision Submitted : April 17, 2019

ABSTRACT

A rotating wheel experimental facility was developed to investigate incompressible Rayleigh Taylor instability in elastic-plastic materials. A soft-solid (mayonnaise) was chosen as the elastic-plastic material for experiments; material properties that include shear modulus and yield strength were fully characterized using a vane-spindle type rheometer. Initial perturbations of varying amplitudes and wavelengths were generated on the interface of the soft solid using sinusoidal cutting guides. A backlit imaging technique was used in conjunction with a high-speed camera to track the motion of the interface at various phases of the instability. Results for both two- and three-dimensional perturbations were compared to study the acceleration required for instability and the growth after the interface yielded. Exponential growth rates were observed after instability was reached with trends of increasing growth rates for lower initial amplitudes. It was found that the acceleration required for instability increased when initial amplitude and wavelength decreased. Three-dimensional interfaces were found to be more stable. For both cases, a decrease in initial amplitude produced a more stable interface that increased the threshold acceleration required for the instability. Critical amplitude conditions for instability were calculated and compared with various analytical models and other experimental results.

I. INTRODUCTION

Rayleigh-Taylor instability (RT/RTI) [1, 2] occurs between materials of dissimilar densities when the density and pressure gradients are in opposite directions, creating an unstable stratification. The instability causes the light material (ρ_2) to accelerate the heavy material (ρ_1), and small perturbations of initial amplitude (ξ_0) and wavelength (λ) at the interface grow and interact eventually becoming turbulent in case of fluids [3]. The growth of an RT unstable interface can be classified into various stages based on the amplitude growth with time [3-6]. According to linear stability theory [4], at small amplitudes ($0.1\lambda < \xi < 0.4\lambda$) the growth over a time t' is exponential such that $\xi = \xi_0 \exp(\gamma t')$, the growth rate (γ) is defined by:

$$\gamma = \sqrt{A_t k a}, \quad (1)$$

where k ($=2\pi/\lambda$) is the wavenumber, a is the acceleration at the interface and $A_t = (\rho_1 - \rho_2)/(\rho_1 + \rho_2)$ is a non-dimensional density difference (Atwood number) between the two materials. RTI occurs in several natural and industrial processes - the atmospheric instability associated with cold air overlaying warm air in the atmosphere, or similar situations with cold and warm water in oceans, rivers or estuaries; in gas bubbles formed during an underwater nuclear explosion; in the ionosphere layer of the atmosphere due to solar radiation; buoyant jets; in finger-like ejecta of stellar materials present in the remnants of a young supernova; in the formation of salt domes under the Earth's crust that occurs over millions of years; and, in the implosion phase of an inertial confinement fusion (ICF) capsule, where RT mixing is formed at high Atwood numbers [7, 8]. Large density gradients in these applications lead to large differential material (fluid or solid) accelerations that give rise to the RT instability. During the last 70 years, RTI has been the subject of numerous experimental [9-13], numerical [3, 14] and theoretical investigations [4, 15]. A comprehensive analysis of these studies can be found in a

recent two-part review by Zhou [16, 17]. However, the majority of these studies focused primarily on applications that involve two Newtonian fluids involving different thermo-physical properties (density and viscosity).

Much less effort has been dedicated to RTI in materials with significant resistance to yield even though they play a significant role in various problems in geophysics [18], astrophysics [19, 20], high-energy density physics (HEDP) [7, 8, 21-26] and in some industrial processes such as explosive welding. The understanding of RTI in accelerated solids or non-Newtonian media has been very limited because instability evolution is governed by the nonlinear constitutive equations that describe the mechanical properties of the solids, namely, elastic-plastic (EP) properties that exhibit both viscous and elastic characteristics under deformation and exhibit time-dependent strain. Miles [27] performed the first theoretical study of Taylor instability in solids using an accelerated (flat) metal plate of finite thickness. The RT problem was solved analytically under the assumption of a single degree of freedom incompressible flow by solving the Prandtl-Reuss constitutive equations for the limiting cases of infinitesimal perturbations and rigid plastic flow (yield stress/shear modulus $\rightarrow 0$). This methodology was extended by Robinson and Swegle [28, 29] using numerical solutions. Drucker [30, 31] extended the theory to determine the critical amplitude above which large plastic deformation occurred in the solid; the critical amplitude was found to be independent of the wavelength for short wavelength perturbations on the interface. Parallel work on the analysis of linear stability problem for an inviscid fluid-metal interface was conducted by Bakhrakh and Kovalev [32, 33]; the work was originally published in Russian and later translated to English in 1997. The Russian authors used normal modes analysis for two-dimensional (2-D) disturbances to derive an equation for the growth rate of the instability as a function of wavenumber k . A

detailed historical brief on the evolution of the analytical theory for RT in solids can be found in Terrones [34].

There has been a handful of reported experiments [35-41] to characterize RTI in EP materials. The first experiment to study RT-strength was performed by Barnes et al. [35] at Los Alamos National Laboratory using aluminum and stainless steel plates with an initial sinusoidal perturbation machined on them. Due to the high yield strength of metals ($\sim 10^8$ Pa), high explosives were used to create a large pressure gradient. The plates were accelerated by generating a driving pressure ~ 10 GPa with ξ_0 ranging from 0.051 mm - 0.1015 mm and with initial λ of 5.08 mm for all but one experiment. The experimental results were compared with a two-dimensional Lagrangian EP code and matched well with a yield strength equivalent to the dynamic yield strength (Y^o). However, varying the shear modulus (G) had little effect on the numerical results. Barnes et al. [35] proposed that Y^o , instead of G , was the dominant property in determining RT-strength and the classical inviscid growth rate was modified to incorporate effects of material strength as:

$$\gamma_F = \left[k A_t a - F(Y^o, \lambda, A_t) \right]^{\frac{1}{2}}, \quad (2)$$

where F is a linear function of Y^o with a slope dependent upon λ and A_t . They also observed that the growth of the instability was inhibited by material strength when a shorter wavelength (2.54 mm) was used and this was considered to be analogous to the case of RTI in fluids where viscosity dampens out the growth of small wavelength perturbations. Drucker [30, 31] used a two-dimensional perfectly plastic model to provide an alternative theoretical analysis of the experimental results of Barnes et al. [35]. The main conclusion was the presence of a threshold value (depending on the dynamic yield strength) which is a function of the plate density, acceleration, and initial amplitude. To test the consistency of their conclusions and to validate

Drucker's findings, Barnes et al. ran additional tests [36] with the same reduced amplitude but a larger initial interface perturbation wavelength than previously used. The experiments found the interface to be stable, confirming the theory that initial amplitude was also a vital parameter along with wavelength in determining the instability threshold as proposed by Drucker. Viscous RTI experiments at high pressure and strain rates have been investigated in the last decade on the Omega Laser facility at the University of Rochester [38]. Using a ramped drive created by the Omega Laser (peak intensity of 2.5×10^{13} W/cm² at $\lambda = 351$ nm), Vanadium target samples were compressed and accelerated quasi-isentropically at ~ 1 Mbar peak pressures while maintaining the sample in the solid state. It was observed that high pressure (~ 1 Mbar), high strain rate ($\sim 10^7$ /s) conditions resulted in a high lattice viscosity which led to a strong stabilization of RTI [38]. A phonon drag mechanism was identified as the primary reason for RT stabilization mechanism at these elevated pressures and strain rates. Park et al. [38] used an effective viscosity due to the phonon drag to interpret the RT stabilization mechanism generating some commentaries amongst researchers if the stabilization mechanism comes from elastic-plastic properties [38, 42].

Due to ambiguity in measurement methods of mechanical properties at these extreme pressures and strain rates, an alternate approach is to use carefully characterized soft-solids (mostly food colloids) as the EP material. Dimonte et al. [37] pioneered this approach by using yogurt as the EP material because of its low yield strength and the flexibility of usage. The linear electric motor (LEM) experiment, which has been used for Newtonian fluids [12] was used to accelerate (vertically) a test section of yogurt and pressurized Nitrogen. The effects of constant and impulsive accelerations were studied in addition to varying amplitude and wavelength requirements for instability. Experiments were performed with both 2D and 3D interfaces with

3D perturbations having a larger range of stability for the same initial conditions. In addition, both elastic and plastic behaviors were observed for impulsive acceleration experiments where the test section was impulsively accelerated to $\sim 100g$'s over 20 ms followed by a phase where the acceleration was completely retracted, and the test section coasted with a constant velocity for an additional 60 ms [37]. Over the range of initial amplitude perturbations that were tested, the instability was observed to grow continuously during the acceleration phase (first 20 ms). The growth ceased once acceleration was removed in the coasting phase (after 20 ms); the behavior in this late phase was strongly dependent on the amplitude of the initial perturbation. For small initial amplitudes, the flow evolved and then elastically recovered; however, at larger amplitudes, the retraction was only partial indicating a plastic transition in response to yield stress. In this work, we describe a novel rotating wheel RTI experiment facility that allows us to expand upon the previous experiments with soft-solids by Dimonte et al. [37]. Our scaled experiments are designed to complement those at high pressures (see Table I for a comparison) because a higher experimental precision is possible in the current experiment since the constitutive properties of the soft-solids are measured independent of the experiment, and the critical parameters can be more easily varied. The current experimental facility allows us to expand our understanding of RT-strength in the linear phase and will complement high-energy-density experiments that have been conducted more recently on laser platforms, providing a useful database for development, validation & verification of RT-strength based models. The remainder of the paper outlines the work completed with the rotating wheel experiment including an overview of the apparatus and material characterization of mayonnaise. Experimental results were compared with previous results and models [27, 30, 31, 37, 43, 44].

II. METHOD

A. Experimental apparatus and diagnostics

A rotating wheel experiment was developed which consists of an aluminum disk, 15.24 cm in diameter, horizontally mounted to a rotating shaft powered by a servo motor (QuickSilver Controls, Inc.); see figure 1 for a schematic of the facility. The test section was constructed from plexiglass (1.3cm thick) with inner dimensions of 60 mm \times 60 mm \times 90 mm ($L \times W \times H$). Mayonnaise was chosen as the EP material; for all our experiments, we used Hellman's Real Mayonnaise which contains 80% vegetable oil, 8% water (both by weight) with other standard ingredients[45]. Mayonnaise in combination with air (used as the light fluid) was put to use in creating non-dimensional density gradient of $A_t \approx 0.997$. The test section was oriented such that the air side was positioned radially outwards, making the initial interface unstable as the resulting acceleration drove the heavy material outwards. The experiment was accelerated using a linear ramp profile and is capable of reaching 60 m/s² in 60 seconds. A high-speed camera (Photron Fastcam Model 1024 PCI) was mounted above the center of the disk and was operated at 500 frames/second (shutter speed= 1/2000s, $f/7$ aperture setting, and 512 \times 512 image resolution) to capture the instability growth. The camera was operated in *end trigger* mode, where images were stacked internally in the memory buffer ensuring the most recent snapshots from the time recording stopped were preserved. NI-LabVIEW[®] was used to control both the motor and the camera while acquiring data for the experiment. To continuously capture images during acceleration, the optical setup consisted of the high-speed camera, light source, and a mirror assembly. The mirror assembly used two mirrors angled at 45°, positioned at the center of rotation and over the container, to project the image of the rotating test section upwards at the center of the disk. The light source consisted of an array of high power LEDs, housed in a container below the harnessed test section to provide backlight imaging for the experiment.

Figure 2 (a) shows a sample experimental image taken at the start of the experiment; the bright portion in the image is air; while mayonnaise, which does not allow light to pass through, appears dark. The first step in defining the initial conditions at the solid-air interface is to fill the lower half of the test section to about ~ 10 mm above the container height. An initial interfacial perturbation in the shape of a sinusoid was applied to mayonnaise by using cutting guides that were precisely machined with curvature $x = \xi_i \cos\left(\frac{2\pi}{\lambda} y\right)$ using a three-axis CNC machine. Fig. 2(b) shows a 3D interface with $\lambda = 60$ mm and $\xi_i = 4$ mm; a corresponding 2D interface of the same wavelength and amplitude is shown in fig.2 (c). The 2D interface is created by holding a pair of cutting guides against the parallel test section walls while removing the excess material. To create a 3D interface, the cutting guides were used to remove material in two mutually perpendicular directions (see fig. 2d). Different sets of cutting guides were precisely machined using a three-axis CNC machining center; in total, five pairs of cutting guides were created with a combination of ten unique interfaces consisting of both 2D and 3D perturbations. To avoid wall effects for 2D perturbations, the interface was shortened ~ 3 mm from the walls on both sides by removing extra material in the y -direction of the test section. For all experiments reported in the manuscript, the time span between defining the initial conditions and running the experiment was less than 5 minutes to avoid any plastic deformation of the specimen.

B. Image processing

The image processing toolbox in MATLAB was used to post-process images of the test section acquired by the high-speed camera. Each raw image was corrected for rotation; the *edge* function and standard Hough Transform [46] were used to determine straight lines from the most distinct edges of the image. The *edge* function transforms a grayscale image into a binary image

where ones represent a pixel location of an edge and zeros are placed everywhere else. A Canny method was used to search for the edges of the image, and determine the local maxima of the gradient from the derivative of a Gaussian filter. After the edges were detected, the standard Hough Transform was used to detect the lines located in the binary image. The peaks of the Hough transform matrix were located and limited by a threshold at which values of the matrix were considered peaks and by a maximum number of peaks. From these peaks, the endpoints for the lines were determined. The corresponding angle between lines determined the amount of rotation required for each image. Figures 3(a) & (b) show an original image of the test section and the resulting edges detected to use for rotation correction. Additionally, the image was cropped to include only the inside of the container to aid in tracking the growth of the amplitude peak with respect to time. After cropping, the image size was reduced from 160 mm × 160 mm to 56 mm × 85 mm due to the rectangular shape of the test section; the peak amplitude was measured from this image based on pixel intensity. A deviation angle was estimated between the centerline in an axial direction (OA) and the line joining (OA') the peak and center as shown in Fig.3c-d. The deviation angle was measured at each time instant for different initial conditions, and the amplitude OA' was used for estimating the growth of the material. The magnitude of the asymmetry is reported in Table II where the maximum deviation angle is reported. It is observed that the deviation increases by a factor of two upon reduction of the initial amplitude for both 2D and 3D perturbations. The deviation is slightly higher in 2D perturbations compared to 3D as the mass of soft solid at the interface is higher in case of 2D perturbations.

III. RESULTS

A. Material characterization

Mayonnaise, an oil-in-water emulsion, was selected as the EP material because it possesses elastic properties that can exhibit growth under accelerations while still maintaining a finite yield strength [47]. The material density (ρ), tensile yield strength (Y), and shear modulus (G) were measured to aid comparison with previous experimental results[35-37] and various analytical models [15, 48]. The density of mayonnaise, determined experimentally by the amount of oil displaced, was found to be $858 \pm 86 \text{ kg/m}^3$ at $\sim 25^\circ \text{ C}$ based on an average of eight independent measurements [49]. Since mayonnaise behaves as a solid as well as non-Newtonian shear-thinning fluid based on the applied stress [47, 50], a Kinexus pro+ rheometer was used to determine Y and G . A vane spindle geometry (Model # 4V14) with 4 blades (diameter = 0.014 m & height = 0.061m) was used in the controlled rate mode to measure torque (T). The shear stress (τ) was calculated from the measured torque for a stress-strain curve using:

$$\tau = \frac{2}{\pi D^3} T \left[\frac{L}{D} + \frac{1}{3} \right]^{-1}, \quad (3)$$

where L and D were the vane spindle length and diameter respectively [50, 51]. The wall slippage phenomenon observed in the vane-cylinder assembly result in large uncertainties of torque readings in the controlled shear rate mode and leads to early disruption of molecular structure in a colloidal dispersion like mayonnaise. To curtail wall slippage effects, it is a common practice to use a cup diameter that is roughly twice as large or greater than the vane diameter [51]. All measurements reported in our studies use a vane spindle of diameter 0.014m in a smooth-walled cup of diameter 0.0275 m to ensure that the effects of wall slippage are minimal. In addition, a fresh sample of mayonnaise was used for each test; a batch was rejected and not used in the instability experiments if the properties deviated more than 5%. The yield stress (Y) of mayonnaise was estimated by using the shear rate ramp method, in which the shear

rate ($\dot{\gamma}$) is increased linearly to a desired magnitude over a specified time interval. Two test cases, one at $\dot{\gamma} = 25 \text{ s}^{-1}$ (where $\Delta t = 60 \text{ s}$), and other at $\dot{\gamma} = 50 \text{ s}^{-1}$ (where $\Delta t = 120 \text{ s}$) were chosen since these magnitudes replicate the shear rates typically observed in our rotating wheel experiment. The shear yield stress (τ_o) can be determined either by extrapolation of shear stress for zero shear rate [52] or by considering maximum stress observed in a shear rate ramp method [49]. Here, we report the final value of shear yield stress (τ_o) by calculating the mean of shear stress at zero shear rate obtained by extrapolation and maximum stress observed in the shear stress-shear rate plot. Figure 4a depicts a shear stress-shear rate plot for a linear shear rate ramp test at $\dot{\gamma} = 25 \text{ s}^{-1}$. The tensile yield strength was determined from shear yield strength as $Y \approx \tau_o \sqrt{3}$; an assumption similar to those made in prior studies involving soft materials like yogurt[37]. The average tensile yield strength for a shear rate of 25 s^{-1} was estimated as $354 \pm 38 \text{ Pa}$. The tensile yield strength increased slightly to a value of $358 \pm 32 \text{ Pa}$ upon doubling the shear rate to 50 s^{-1} . The apparent viscosity (plotted as an inset to fig.4a) demonstrates a shear thinning behavior at shear rates beyond 1 s^{-1} . The shear modulus was determined using an amplitude sweep test at a fixed frequency[53]. This test is usually used to estimate the linear viscoelastic region in which the modulus remains constant. Vane spindle (4V14) geometry is used in this test for two different frequencies (1 Hz and 5 Hz). The value of shear modulus, which is equivalent to storage modulus resulted from the tests is $G = 985 \pm 24 \text{ Pa}$. The plots of storage (G') and viscous (G'') moduli against complex shear strain for different frequencies were shown in fig. 4b. The presence of surface tension in the material reduces the RTI-growth rate[43, 54]. The surface tension effects can be neglected if the Bond number (Gravitational forces/surface tension forces $= \Delta\rho g L^2 / \sigma$) is greater than 1. Here, $\Delta\rho$ is the density difference at the interface, g is the acceleration at the interface which typically ranges between, L is the characteristic length

equivalent to the width of the test section and σ is surface tension of the material-air interface. In the current experimental study, the gravitational force per unit length ($gL^2\Delta\rho$) is $\approx 10^2$ N/m. The coefficient of the surface tension of emulsions typically in the order of 10^{-1} N/m [55]. The surface tension coefficient (σ) of mayonnaise was measured with a tensiometer using a Du Noüy ring method [56] and was found to be 0.56×10^{-1} N/m. Surface tension effects were thus neglected in the present study as the corresponding Bond number is $\approx 10^3$.

Given the experimental conditions, the fluidity of the material is characterized by performing a frequency sweep test and to estimate G' and G'' . In these tests, the time-dependent viscoelastic properties of the material are evaluated by varying the oscillation frequency at a constant strain amplitude. The frequency is increased logarithmically over a range of 0.001 - 10 Hz as the shear rates observed in the experiments lies within this range. For the current vane and cup geometry, a frequency of 1 Hz is equivalent to the shear rate of 18 s^{-1} . As shown in fig. 4c, $G' > G''$ throughout the range of frequency tested; this justifies the solid-like behavior of material [57]. Hence, the validity of an approximate equation, $Y \approx \tau_o \sqrt{3}$ close to von Mises yield criterion in the existing range of shear rates observed in current experiments is reasonable. The results for shear yield stress (τ_o) ranges between 180 - 220 Pa. The shear modulus was dependent on the frequency with G ranging from 955 Pa to 1010 Pa. The results were compared with the storage (elastic) modulus estimations from the oscillatory shear tests for mayonnaise with 80% oil concentration reported by Liu et al. [58], and they are observed to be consistent and within the specified range. The material properties considered in the analysis with the current experiment results are: $\rho = 858 \pm 86 \text{ kg/m}^3$, $Y = 356 \pm 35 \text{ Pa}$, and $G = 985 \pm 24 \text{ Pa}$.

B. Instability acceleration threshold

The experimental results obtained from instability tests using the rotating wheel experiment are discussed. The interfacial perturbations studied (shown in fig. 2e) were either two-dimensional (2D) or three-dimensional (3D), and initial amplitudes (ξ_i) ranged from $w/60$ to $w/10$ while the perturbation wavelengths (λ) ranged from $w/4$ to w , where w is the width of the test section (60 mm). For each perturbation tested, at least four cases were run and the data presented is the average of four experiments.

In the instability tests, the test section is accelerated to determine the instability threshold acceleration (a_o) at which the sample yields. The dimensionless interfacial amplitude [$\log_{10}(\xi/\xi_i)$] is plotted as a function of time for an experimental run with initial conditions, $\xi_i = 4$ mm & $\lambda = 60$ mm is shown in fig. 5. The data is observed to be continuous over the EP phase; upon transition to instability, the perturbation grows rapidly as the driving acceleration exceeds the yield strength of mayonnaise. Two different timescales are defined to allow comparison; an experiment time (t) was the timing of the motor such that $t = 0$ indicated the beginning of an experiment and instability time (t') was the time after the sample yielded. During the acceleration, the observed interface growth can be broken up into two representative regimes: (a) *Elastic-Plastic growth* characterized by very slow increase in the amplitude; if the acceleration is withdrawn, the sample retracts to an amplitude $> \xi_i$ showing elastic-plastic deformation; and, (b) *Instability growth* where the sample undergoes rapid growth beyond a critical amplitude of ξ_o . The general distinction between elastic-plastic growth and instability growth can be made in terms of strain rate. The strain rates in the elastic-plastic growth phase are typically $\approx 10^{-1} \text{ s}^{-1}$ whereas the strain rates in the instability regime are always higher than 10 s^{-1} . A 100-fold difference in the strain rates is generally observed between these two growth phases. However, the exact location of the transition point is required to determine the threshold parameters, a_o &

ξ_0 . Attempts to non-dimensionalize the perturbation amplitude using the initial amplitude (ξ_i) and the time by a/λ did not result in any global scaling for these experiments; we choose to report dimensional values for all our experiments in the instability regime.

A single linear or non-linear regression model may not be adequate to analyze the complex relationship between an independent variable (e.g., driving pressure rise time, t) and a dependent variable (e.g., perturbation amplitude, ξ). The piecewise (segmented) regression is a special case of switching regression, which is generally used in statistical analysis of continuous data [59-61]. The implementation of the piecewise linear regression method to our experimental data using two linear curves was particularly motivated from a rheological study to determine yield stress of soft solids by Dapčević et al.[62]. Two linear fits were used in their study to distinguish the solid and viscous behavior of soft-solid in a stress ramp test which is analogous to driving pressure (acceleration) increase with time in our experimental study. Likewise, the rapid growth in instability regime is differentiated from the significantly lower growth rate of perturbation in the EP phase. In the initial iteration, the experimental data is divided into two subsets, and a linear curve is fitted to each subset. The number of iterations is entirely dependent on the number of experimental data points in the amplitude vs. time plot in the instability growth phase. Consequently, in each iteration, we find the distinct coefficients of determination (R^2_{EP} & R^2_{IN}) of the two linear fits for the corresponding subsets. The best linear fits effectively differentiate the amplitude trend for which the sum of coefficients of determination ($R^2_{EP,max} + R^2_{IN,max}$) would be maximum. The amplitude and time at the transition point in the iteration with best linear fit are considered as the instability amplitude (ξ_0) and the instability time, $t' = 0$ as shown in the inset of fig.5. The peak amplitude at the start of instability (ξ_0) was used to curve fit an exponential growth rate γ defined by eq.1.

Table II shows a detailed list of experiments performed for the instability test. To study the effect of amplitude on the instability acceleration, the perturbation amplitude was varied from ~ 1 mm to 6 mm while the wavelength remained constant at 60 mm; both 3D and 2D perturbations were studied. Similarly, to study the effect of wavelength, the initial amplitude was held constant at ~ 4 mm while the wavelength ranged from 15 mm to 60 mm for 3D and 2D. The ratio of perturbation wavelength to the width of the test section in our study ranges between 0.25 – 1.0 and is similar to values used in other experiments[37, 40, 41]; for example, the LEM experiments [37] have a wavelength/width ratio of 0.5-1.0. Previous research by Swegle and Robinson [28] to study the effects of initial conditions on RT-strength, numerically, used a Lagrangian finite difference wave code to indicate that *both* initial amplitude and wavelength determined a stability boundary. Piriz et al. [48] used an analytical model and finite element analysis software ABAQUS to determine a relationship between the initial perturbation and material properties with the stability boundary described by Swegle and Robinson. Simulation results agreed with the model and showed that lower initial amplitudes and wavelengths were more stable for equivalent material properties and accelerations. The following instability tests were used to validate these initial condition trends further.

i. Effect of amplitude and estimating the critical amplitude

For 3D perturbations, Figure 6 (a)-(d) show the experimental images for the different initial amplitudes that were tested with different initial amplitudes. For each interface, the first image is the initial amplitude (ξ_i) at $t = 0$, and the remaining images highlight the perturbation growth from the start of instability ($t' = 0$) until the peak reached the top of the test section. Qualitatively, the shape of the perturbation growth after the start of instability is similar and independent of initial amplitude. The initial peak grew and, once instability occurred, began to

elongate. Due to the tensile deformation of the mayonnaise, the perturbation began to neck approximately half-way between the top of the peak and center of the test section. For 2D perturbations, the effect of amplitude was investigated using similar initial perturbations (same peak) as 3D. Figure 7(a)-(d) display the experimental images for 2D perturbations with the largest wavelength on top followed by the intermediate and smallest amplitudes. Unlike the amplitude variation experiments (see images in fig. 6), the interface shape for $\xi_i = 2$ mm and 1 mm did not follow the same profile as other perturbations. Instead of a distinct peak growing, the interface grew as if the whole sample was yielding. Volume was conserved under these conditions although it is not possible to quantify this as mayonnaise is opaque and the images and depth-integrated 2D realization of the instability occurring in the 3D enclosure. For each instability test, starting at $t' = 0$, the peak amplitude was plotted with respect to time until the peak reached the top of the test section. Figure 8 shows sample peak amplitude growth corresponding to an approximate ξ_i of 6 mm, 4 mm, 2 mm, and 1 mm, respectively, for 3D interfaces. The interface amplitude data in the instability regime was used to calculate an exponential growth rate constant (γ). For each perturbation, at least four cases were tested, and the results were averaged to account for random error. Table III displays the instability acceleration (a_o) and experimental growth rate (γ) calculated for each perturbation. For both 3D and 2D perturbations, lower initial amplitudes required a larger acceleration to reach instability, agreeing with previous research [28, 37, 48]. When comparing the 2D and 3D instability accelerations for the same initial perturbation, results indicated 3D interfaces were more stable than 2D. Dimonte et al. [37] found the same trend with experimental results using yogurt. For 3D perturbations, the calculated growth rate is observed to increase from ~ 10 s⁻¹ to 25 s⁻¹ as the initial amplitudes decrease from 6mm to 1mm. Similarly, exponential growth rates for 2D

perturbations increased from $\sim 12 \text{ s}^{-1}$ to 31 s^{-1} with decreasing initial amplitude. However, the large growth rates for $\xi_i = 2 \text{ mm}$ & 1 mm should be viewed with caution due to the unique profile of the perturbation growth in the experimental images (see fig. 8). When estimating the growth rates for these experiments, care was taken to ensure that the data used was in the linear phase. Linearization is justified if the surface displacement and slope are small in dimensionless terms; a condition that is enforced mathematically as $d\xi/dz \ll 1$ and $g\xi/U^2 \ll 1$ [63] where z is length scale in the direction of interface growth and U is the perturbation velocity. These constraints hold in throughout the instability regime from the onset for all reported experiments in this paper.

Previous research [27, 30, 31, 37] has determined a critical amplitude (ξ_{crit}) based on acceleration and material properties where perturbation growth is unstable for $\xi_o > \xi_{crit}$. Miles [27] first derived a critical amplitude for RT-strength by modifying the classic RT growth equation $\xi = \xi_o \exp(\sqrt{A_i k a t})$ to account for the effects of material strength using a rigid-plastic model with Prandtl-Reuss constitutive equations and $\rho_2 = 0$, where the critical amplitude for the model was given by

$$\xi_{crit} = \frac{4Y}{\sqrt{3\rho a}}. \quad (4)$$

Drucker [30, 31] also proposed an RT growth equation for strength where the effects of yield strength were emphasized. The model was based on the theory of significant growth occurring if the elastic limit of the material property was exceeded making the yield strength a more dominant factor than the shear modulus, and the critical amplitude was

$$\xi_{crit} = \frac{2Y}{\rho a} \quad (5)$$

Comparisons with the experimental work of Barnes et al. [35] agreed well with Drucker's model. A third definition for ξ_{crit} was proposed from 2D experimental yogurt results by Dimonte et al. [37]

$$\xi_{crit} = \frac{Y}{\rho a} \quad (6)$$

The current ξ_{crit} for instability was determined based on a curve fit of the experimental data where the perturbation amplitude was varied (at a constant wavelength) for both 2D and 3D initial perturbations; the results are then compared with the previous results in Eqs. (4)-(6). The averaged results in Table III were plotted to provide a relationship between ξ_o and $Y/\rho a$, as shown in fig. 9. From the results, ξ_{crit} , was found to be $\sim 1.8Y/\rho a$ for 3D perturbations using a linear curve fit with a resulting $R^2 = 0.83$. For 2D perturbations, ξ_{crit} was $\sim 1.4Y/\rho a$ with $R^2 = 0.81$. Table IV compares the current ξ_{crit} with previous results. Both analytical methods found a higher ξ_{crit} , while the current work and experimental results by Dimonte et al. [37] found lower values for ξ_{crit} . When comparing the results for the current work, ξ_{crit} for 3D and 2D experimental results were in between the Drucker model [30, 31] and the 2D results of Dimonte et al. [37].

ii. Effect of wavelength

To study the effect of wavelength, fig. 10 (a)-(b) show experimental images of 3D perturbations for $\xi_i = 4$ mm with $\lambda = 30$ mm and $\lambda = 15$ mm, respectively. The first image is the

initial interface, and the remaining images highlight the instability and amplitude growth, similar to fig. 6 of experimental images of the amplitude effect study . Figure 6 (b) shows experimental images for the largest wavelength ($\lambda = 60$ mm). Comparable to the effect of amplitude results, the peak amplitude grew, and necking occurred due to the material's deformation. For the smallest wavelength perturbation ($\lambda = 15$ mm), the necking increased until a pinch off occurred and the resulting peak detached as a bubble. Similar detachment would be expected for larger wavelengths if the test section was taller. Figure 11 (a)-(b) highlight experimental images for 2D perturbations where profile growths were qualitatively the same as 3D results, see fig 7(a) for 2D perturbations with $\lambda = 60$ mm. Sample peak amplitude growth for 3D perturbations corresponding to an approximate λ equal to 60 mm, 30 mm, and 15 mm are shown in fig. 12. The peak amplitude at the start of instability (ξ_o) increases with wavelength. For all wavelengths tested, an exponential growth rate was observed with slightly higher values for $\lambda = 15$ mm, due to the spike beginning to detach from the interface. The experimental results for effect of wavelength were averaged to account for random error as displayed in Table V. The acceleration required to reach instability increased with decreasing wavelength, agreeing with previous research [28, 48]. The exponential growth rate varied from $\sim 13 \text{ s}^{-1}$ to 27 s^{-1} for 3D and from $\sim 15 \text{ s}^{-1}$ to 28 s^{-1} for 2D, with an increase in growth rate as the perturbation wavelength decreased. Analogous to the effect of amplitude results, 2D perturbations were less stable than 3D perturbations for the same initial conditions.

C. Growth rate comparison with models for RT-strength

Previous models for RT-strength have modified the classical growth rate to account for effects of yield strength as shown in Eq. (2) [35]. Others have studied the effects of viscosity and

surface tension [15, 43, 44, 64] on RT-strength growth rates. Analysis by Miles and Dienes [44] determined an approximate exponential growth rate based on dynamic viscosity as

$$\gamma_{\mu} = 0.4(\rho\alpha^2/\mu)^{1/3}, \quad (7)$$

where the effects of surface tension can be neglected for $kh \gg 1$; here h is the slab/plate thickness. The growth rates for 2D perturbations using yogurt and the LEM experiment [37] agreed well with Eq. (7) resulting in $\gamma \sim 100 \text{ s}^{-1}$ and using a measured dynamic viscosity of $\mu = 5 \text{ Pa s}$. Bellman and Pennington [43] modified the classic growth for RT-strength to determine the effects of surface tension and viscosity. Results showed that both parameters reduced the growth rate. Furthermore, viscosity decreased the growth rate as the wavelength approached zero. The simplified case for pure viscosity ($kh \gg 1$) was governed by:

$$\gamma_v = -k^2\nu + \sqrt{k^4\nu^2 + A_r ak}, \quad (8)$$

where ν is the kinematic viscosity. Mikaelian [15] found the same result when solving the momentum equation for RT instability by setting the surface tension coefficient to zero. Colvin et al. [64] used a similar approach as Mikaelian, but represented surface tension as a function of shear modulus ($T \rightarrow G/k$). For fully plastic flow, when the pressure applied is greater than the yield strength, $G = 0$ and the viscous growth rate by Colvin et al. matches Eq. (8), for large values of kh . Additionally, Colvin et al. determined an equivalent plastic kinematic viscosity based on strain rate ($\dot{\epsilon}$) and the von Mises criterion as

$$\nu_{EP} = \frac{Y}{\sqrt{6\rho\dot{\epsilon}}} \quad (9)$$

For both 3D and 2D perturbations, the measured growth rates were compared with theories for

RT exponential growth rate ($\gamma = \sqrt{A_1 k a}$) for inviscid fluids. Using $k = \sqrt{(2\pi/\lambda_y)^2 + (2\pi/\lambda_x)^2}$, a 3D perturbation with $\lambda = 60$ mm has a wavenumber of $k \sim 148$ m⁻¹ and calculated the classical growth rate of ~ 74 s⁻¹ to 103 s⁻¹ which varies with the initial amplitude, using the instability accelerations determined from experiments. The current measured experimental growth rates were ~ 11 s⁻¹ to 27 s⁻¹ for $\lambda = 60$ mm. The difference in rates is expected because linear stability theory does not account for the viscous effects of the EP material in RT-strength. For comparison, the experimental growth rate results with yogurt by Dimonte et al. [37] were $\sim 40\%$ of linear stability theory for similar perturbations. Experimental growth rates were compared with the viscous models of Miles and Dienes [44] (γ_μ) and Bellman and Pennington [43] (γ_ν) as outlined in Eqs. (7) and (8), respectively. The kinematic viscosity (ν) was calculated with Eq. (9)

where $\dot{\xi}$ was estimated from the average rate of change in peak amplitude for $t' \geq 0$ as $\frac{1}{\xi_o} \frac{\Delta \xi}{\Delta t}$.

Applying the material properties for mayonnaise and using the average instability acceleration for 3D perturbation $\lambda = 60$ mm $\xi_i = 4$ mm ($a_o = 48.55$ m/s), Eq. (8) yielded a growth rate of ~ 21 s⁻¹. Current experimental results for the same perturbation measured ~ 13 s⁻¹ for exponential growth. Using Eqs. (7) and (8), growth rates for both models were calculated for each interface and compared with the measured experimental γ for the effect of amplitude and wavelength results as shown in Tables VI and VII respectively. To calculate dynamic viscosity (μ) for Eq. (7), the definition for kinematic viscosity, Eq. (9), was used resulting in dynamic viscosity values ranging from ~ 3 to 8 Pa s due to the variance in strain rate for the different instability accelerations. Because mayonnaise is a non-Newtonian fluid, a change in viscosity is expected with varying strain rate. Both viscous models for growth rates showed an increase in the calculated rate as the initial amplitude decreased. The change in viscous models' growth rates

was due to the change in instability acceleration and strain rate observed in the mayonnaise experiments. With the decrease in ξ_i , the rate of increase of γ_v is significantly higher ($\sim 350\%$ in 3D cases & $\sim 420\%$) than γ_μ ($\sim 130\%$ in 3D cases & $\sim 160\%$ in 2D cases). Overall, measured growth rates were found to be lower than both viscous growth rate models irrespective of initial amplitude. Similar to the effect of amplitude results, the experimental growth rates were always lower than predicted γ_μ values for any given wavelength of the interface. From the effect of wavelength results, it is observed that growth rates measured experimentally and predicted by Miles and Dienes' model[44] increase with a decrease in wavelength. However for $\lambda = 15$ mm, Bellman and Pennington model[43] underpredicts the growth rate in comparison to current experiment growth rates.

IV. CONCLUSIONS

To study the effect of initial amplitude and wavelength on RT-strength instability, different sinusoidal perturbations were formed on an elastic-plastic material (mayonnaise) and accelerated in a test section, with air as the light fluid, using a novel rotating wheel experiment. For the effect of amplitude, the initial conditions were varied from 1 mm to 4 mm while the wavelength was varied from 15 mm to 60 mm to study the effect of wavelength. Results for both 2D and 3D perturbations showed a decrease in initial amplitude and wavelength produced a more stable interface thereby increasing the acceleration required for instability. Comparing instability accelerations demonstrated 3D perturbations were more stable than 2D for equivalent initial conditions. Critical amplitude conditions for instability were calculated and compared with previous models and experimental results. For 2D perturbations, experimental results matched with Drucker's model [30, 31], $1.4Y/\rho a$, while 3D results were $1.8Y/\rho a$, in between the 3D experimental results of Dimonte et al. [37] and Drucker's model[30, 31]. The growth observed

after reaching the instability were exponential with calculated rates $\sim 13 \text{ s}^{-1}$ to 27 s^{-1} and trends of increasing growth rates for lower initial amplitudes and wavelength. Results indicated that growth rates were slightly higher for 2D perturbations compared to 3D perturbations. For both 2D and 3D perturbations, experimental growth rates were found to be lower than growth rates estimated by models developed by Bellman and Pennington [43] & Miles and Dienes[44] in all the cases except for 15 mm wavelength case.

Acknowledgments

Arindam Banerjee would also like to devote this paper to the memory of Dr. Malcolm J. Andrews. This work is funded through a Department of Energy-Stewardship Science Academic Alliance Grant # DE-NA0003195 and a Los Alamos National Laboratory subcontract #370333. Pamela Roach would like to support the NSF Graduate Research Fellowship program for financial support for this project.

REFERENCES

- [1] L. Rayleigh, Investigation of the equilibrium of an incompressible heavy fluid of variable density, Proceedings of Royal Society of London, 14 (1884) 170-177.
- [2] G.I. Taylor, The instability of liquid surfaces when accelerated in a direction perpendicular to their planes I. , Proceedings of Royal Society of London Series A, 201 (1950) 192-196.
- [3] D.L. Youngs, Numerical simulation of turbulent mixing by Rayleigh-Taylor instability, Physica D, 12 (1984) 32-44.
- [4] S. Chandrasekhar, Hydrodynamic and hydromagnetic stability, 2nd ed., Dover Publications, New York, 1981.
- [5] D.H. Sharp, An overview of Rayleigh-Taylor instability, Physica D, 12 (1984).
- [6] D.J. Lewis, The instability of liquid surfaces when accelerated in a direction perpendicular to their planes II. , Proceedings of Royal Society of London Series A, 202 (1950) 81-96.

- [7] R. Betti, M. Umansky, V. Lobatchev, V.N. Goncharov, R.L. McCrory, Hot-spot dynamics and deceleration-phase Rayleigh-Taylor instability of imploding inertial confinement fusion capsules, *Physics of Plasmas*, 8 (2001) 5257-5267.
- [8] S. Atzeni, J. Meyer-ter-Vehn, *The physics of inertial fusion : beam plasma interaction, hydrodynamics, hot dense matter*, Clarendon Press 2004.
- [9] M.J. Andrews, D.B. Spalding, A simple experiment to investigate two-dimensional mixing by Rayleigh-Taylor instability, *Physics of Fluids A*, 2 (1990) 922-927.
- [10] A. Banerjee, W.N. Kraft, M.J. Andrews, Detailed measurements of statistically steady Rayleigh-Taylor mixing layer from small to high Atwood numbers, *Journal of Fluid Mechanics*, 659 (2010) 127-190.
- [11] S.B. Dalziel, P.F. Linden, D.L. Youngs, Self-similarity and internal structure of turbulence induced by Rayleigh-Taylor instability, *Journal of Fluid Mechanics*, 399 (1999) 1-48.
- [12] G. Dimonte, M. Schneider, Turbulent Rayleigh-Taylor instability experiments with variable acceleration., *Physical Review E*, 54 (1996) 3740-3743.
- [13] D.M. Snider, M.J. Andrews, Rayleigh-Taylor and shear driven mixing with an unstable thermal stratification., *Physics of Fluids*, 6 (1994) 3324-3334.
- [14] G. Dimonte, D.L. Youngs, A. Dimits, S. Weber, M. Marinak, S. Wunch, C. Garasi, A.C. Robinson, M.J. Andrews, P. Ramaprabhu, A. Calder, B. Fryxell, J. Biello, L. Dursi, P. MacNeice, K. Olsen, P. Ricker, R. Rosner, F. Timmes, H. Tofu, Y.-N. Young, M. Zingale, A comparative study of the turbulent Rayleigh–Taylor instability using high-resolution three-dimensional numerical simulations: The Alpha-Group collaboration, *Physics of Fluids*, 16 (2004) 1668-1693.
- [15] K.O. Mikaelian, Effect of viscosity on Rayleigh-Taylor and Richtmyer-Meshkov instabilities, *Physical Review E*, 47 (1993) 375-383.
- [16] Y. Zhou, Rayleigh–Taylor and Richtmyer–Meshkov instability induced flow, turbulence, and mixing. I, *Physics Reports*, 720-722 (2017) 1-136.
- [17] Y. Zhou, Rayleigh–Taylor and Richtmyer–Meshkov instability induced flow, turbulence, and mixing. II, *Physics Reports*, 723-725 (2017) 1-160.
- [18] K.-K. Tan, R.B. Thorpe, Z. Zhao, On predicting mantle mushroom plumes, *Geoscience Frontiers*, 2 (2011) 223-235.
- [19] S.A. Colgate, R.H. White, The hydrodynamic behavior of supernova explosions, *Astrophysical Journal*, 143 (1966) 626-681.
- [20] S.F. Gull, The X-ray, optical and radio properties of young supernova remnants, *Royal Astronomical Society Monthly Notices*, 171 (1975) 263-278.

- [21] S. Atzeni, A. Schiavi, F. Califano, F. Cattani, F. Cornolti, D. Del Sarto, T.V. Liseykina, A. Macchi, F. Pegoraro, Fluid and kinetic simulation of inertial confinement fusion plasmas, *Computer Physics Communications*, 169 (2005) 153-159.
- [22] J.D. Lindl, Development of the indirect-drive approach to inertial confinement fusion and the target physics basis for ignition and gain, *Physics of Plasmas*, 2 (1995) 3933-4024.
- [23] J.D. Lindl, *Inertial confinement fusion: the quest for ignition and energy gain using indirect drive*, Springer, Berlin, 1998.
- [24] S. Nakai, H. Takabe, Principles of inertial confinement fusion-physics of implosion and the concept of inertial fusion energy, *Report of Progress in Physics*, 59 (1996) 1071-1131.
- [25] S. Pfalzner, *An Introduction to Inertial Confinement Fusion*, CRC Press, New York, 2006.
- [26] D.C. Wilson, A.J. Scannapieco, C.W. Cranfill, M.R. Clover, N.M. Hoffman, J. Collins, Degradation of radiatively driven inertial confinement fusion capsule implosions by multifluid interpenetration mixing, *Physics of Plasmas*, 10 (2003) 4427-4434.
- [27] J.W. Miles, Taylor instability of a flat plate, in: *G.A. Report (Ed.)*, 1966.
- [28] J.W. Swegle, A.C. Robinson, Acceleration instability in elastic-plastic solids. I. numerical solutions of plate acceleration, *Journal of Applied Physics*, 66 (1989) 2838-2858.
- [29] J.W. Swegle, A.C. Robinson, Acceleration instability in elastic-plastic solids. II. analytical techniques, *Journal of Applied Physics*, 66 (1989) 2859-2872.
- [30] D.C. Drucker, Taylor instability of the surface of an elastic-plastic plate, *Mechanics Today*, 5 (1980) 37-47.
- [31] D.C. Drucker, A further look at Rayleigh-Taylor and other surface instabilities in solids, *Archive of Applied Mechanics*, 49 (1980) 361-367.
- [32] S.M. Bakhrah, N.P. Kovalev, *Numerical Methods for Solid State Mechanics*, Novosibirsk, 1980.
- [33] S.M. Bakhrah, N.P. Kovalev, Taylor instability in elastic-plastic media, *Proc. of the 5th All-Union Conference on numerical methods for solving elasticity and plasticity theory problems Novosibirsk*, 1978, pp. 22-36.
- [34] G. Terrones, Fastest growing linear Rayleigh-Taylor modes at solid/fluid and solid/solid interfaces, *Physical Review E*, 71 (2005) 036306.
- [35] J.F. Barnes, P.J. Blewett, R.G. McQueen, K.A. Meyer, D. Venable, Taylor instability in solids, *Journal of Applied Physics*, 45 (1974) 727-732.
- [36] J.F. Barnes, D.H. Janney, R.K. London, K.A. Meyer, D.H. Sharp, Further experimentation on Taylor instability in solids, *Journal of Applied Physics*, 51 (1980) 4678-4679.

- [37] G. Dimonte, R.A. Gore, M. Schneider, Rayleigh-Taylor instability in elastic-plastic materials, *Physical Review Letters*, 80 (1998) 1212-1215.
- [38] H.-S. Park, K.T. Lorenz, R.M. Cavallo, S.M. Pollaine, S.T. Prisbrey, R.E. Rudd, R.C. Becker, J.V. Bernier, B.A. Remington, Viscous Rayleigh-Taylor instability experiments at high pressure and strain rate, *Physical Review Letters*, 104 (2010) 135504-135504.
- [39] H.-S. Park, B.A. Remington, R.C. Becker, J.V. Bernier, R.M. Cavallo, K.T. Lorenz, S.M. Pollaine, S.T. Prisbrey, R.E. Rudd, N.R. Barton, Strong stabilization of the Rayleigh–Taylor instability by material strength at megabar pressures), *Physics of Plasmas* (1994-present), 17 (2010) 056314.
- [40] S. Mora, T. Phou, J.-M. Fromental, Y. Pomeau, Gravity Driven Instability in Elastic Solid Layers, *Physical Review Letters*, 113 (2014) 178301.
- [41] I. Maimouni, J. Goyon, E. Lac, T. Pringuey, J. Boujlel, X. Chateau, P. Coussot, Rayleigh-Taylor Instability in Elastoplastic Solids: A Local Catastrophic Process, *Physical Review Letters*, 116 (2016) 154502.
- [42] A.R. Piriz, J.J. López Cela, N.A. Tahir, Comment on "Viscous Rayleigh-Taylor Instability Experiments at High Pressure and Strain Rate", *Physical Review Letters*, 105 (2010) 179601.
- [43] R. Bellman, R.H. Pennington, Effects of surface tension and viscosity on Taylor instability, *The Quarterly of Applied Mathematics*, 12 (1954) 151-162.
- [44] J.W. Miles, J.K. Dienes, Taylor instability in a viscous liquid, *Physics of Fluids*, 9 (1966) 2518-2519.
- [45] C.K. Dartey, T.M. Trainor, R. Evans, Low cholesterol mayonnaise substitute and process for its preparation, Google Patents, 1990.
- [46] R.O. Duda, P.E. Hart, Use of the Hough transformation to detect lines and curve in pictures, *Communications of the ACM*, 15 (1972) 11-15.
- [47] E. Dickinson, *An Introduction to Food Colloids*, Oxford University Press, United States, 1992.
- [48] A.R. Piriz, J.J.L. Cela, N.A. Tahir, Linear analysis of incompressible Rayleigh-Taylor instability in solids, *Physical Review E*, 80 (2009) 046305.
- [49] G. Dimonte, D. Nelson, S. Weaver, M. Schneider, E. Flower-Maudlin, R. Gore, J.R. Baumgardner, M.S. Sahota, Comparative study of viscoelastic properties using virgin yogurt, *Journal of Rheology*, 42 (1998) 727-742.
- [50] D.B. Genovese, M.A. Rao, Components of vane yield stress of structured food dispersions, *Journal of Food Science*, 70 (2005) 498-504.
- [51] R.P. Chhabra, J.F. Richardson, *Non-Newtonian Flow and Applied Rheology: Engineering Applications*, Elsevier, Hungary, 2008.

- [52] B. Yoo, M.A. Rao, J.F. Steffe, Yield Stress of Food Dispersions with the Vane Method at Controlled Shear Rate and Shear Stress, *Journal of Texture Studies*, 26 (1995) 1-10.
- [53] F.A. Morrison, *Understanding Rheology*, Oxford University Press 2001.
- [54] K.O. Mikaelian, Rayleigh-Taylor instability in finite-thickness fluids with viscosity and surface tension, *Physical Review E*, 54 (1996) 3676-3680.
- [55] L. Martinie, H. Buggisch, N. Willenbacher, Apparent elongational yield stress of soft matter, *Journal of Rheology*, 57 (2013) 627-646.
- [56] L.L. Schramm, *Emulsions, foams, and suspensions: fundamentals and applications*, John Wiley & Sons 2006.
- [57] K. Hyun, S.H. Kim, K.H. Ahn, S.J. Lee, Large amplitude oscillatory shear as a way to classify the complex fluids, *Journal of Non-Newtonian Fluid Mechanics*, 107 (2002) 51-65.
- [58] H. Liu, X.M. Xu, S.D. Guo, Rheological, texture and sensory properties of low-fat mayonnaise with different fat mimetics, *Lwt - Food Science and Technology*, 40 (2007) 946-954.
- [59] G.F. Malash, M.I. El-Khaiary, Piecewise linear regression: A statistical method for the analysis of experimental adsorption data by the intraparticle-diffusion models, *Chemical Engineering Journal*, 163 (2010) 256-263.
- [60] S.E. Ryan, L.S. Porth, C. Troendle, Defining phases of bedload transport using piecewise regression, *Earth Surface Processes and Landforms*, 27 (2002) 971-990.
- [61] P. Colella, A Direct Eulerian MUSCL Scheme for Gas Dynamics, *SIAM Journal on Scientific and Statistical Computing*, 6 (1985) 104-117.
- [62] T. Dapčević, P. Dokić, M. Hadnađev, M. Pojić, Determining the yield stress of food products-importance and shortcomings, *Food Processing-Quality and Safety*, 35 (2008) 143-149.
- [63] P.G. Drazin, *Introduction to Hydrodynamic Stability*, Cambridge University Press, Cambridge, 2002.
- [64] J.D. Colvin, M. Legrand, B.A. Remington, G. Schurtz, S.V. Weber, A model for instability growth in accelerated solid metals, *Journal of Applied Physics*, 93 (2003) 5287-5301.

Table I. RT-Strength Experiments

Experiment Facility	EP Material	Yield Strength (Pa)	Light Fluid	Pressure (Pa)	Initial Amplitude (mm)	Initial Wavelength (mm)
HE [35]	1100 Al	30×10^6	Helium	10^{10}	0.051 - 0.1015	2.54 - 5.08
	6061 – T6 Al	250×10^6			0.1015	5.08
	304 SS	300×10^6			0.1015	5.08
HE [36]	1100 Al	30×10^6	Helium	10^{10}	0.051	4.73
Omega Laser Facility [38]	Vanadium	715×10^6	Helium	10^{11}	0.0006	0.06
LEM [37]	Yogurt	340	Nitrogen	$\sim 10^4$	0.66 - 4	30 - 60
Rotating Wheel (Current Work)	Mayonnaise	356 ± 35	Air	$\sim 10^3$	1 - 6	15 - 60

Table II. Details of Instability Tests.

Dimensionality (2D/3D)	Wavelength - λ (mm)	Initial Amplitude - ξ_i (mm)	Maximum Deviation Angle (degrees)
3D	60	5.88 ± 0.13	8.65 ± 1.19
		3.95 ± 0.17	12.25 ± 1.32
		2.88 ± 0.13	13.09 ± 1.33
		1.88 ± 0.17	14.91 ± 2.41
		0.90 ± 0.16	15.80 ± 4.95
	30	3.83 ± 0.17	16.95 ± 1.04
15	3.87 ± 0.18	18.39 ± 1.77	
2D	60	5.76 ± 0.13	7.42 ± 3.19
		3.55 ± 0.18	15.17 ± 1.30
		2.76 ± 0.12	16.62 ± 3.32
		1.63 ± 0.17	19.40 ± 0.46
		0.69 ± 0.16	17.81 ± 1.72
	30	3.52 ± 0.17	19.19 ± 1.24
15	3.48 ± 0.17	20.68 ± 0.34	

Table III. Instability tests – varying the perturbation amplitude.

2D/3D	Initial Amplitude - ξ_i (mm)	Instability Acceleration - a_o (m/s ²)	Instability Amplitude - ξ_o (mm)	Measured Growth Rate - γ (s ⁻¹)
3D	5.88 ± 0.13	36.69 ± 1.85	18.34 ± 0.81	10.86 ± 0.62
	3.95 ± 0.17	48.55 ± 1.71	16.13 ± 0.78	13.32 ± 1.21
	2.88 ± 0.13	57.57 ± 1.96	14.20 ± 0.32	15.78 ± 0.56
	1.88 ± 0.17	65.49 ± 2.23	11.65 ± 1.76	17.79 ± 2.65
	0.90 ± 0.16	71.20 ± 3.22	10.97 ± 1.34	24.34 ± 0.75
2D	5.76 ± 0.13	30.37 ± 0.79	16.99 ± 0.34	11.85 ± 0.57
	3.55 ± 0.18	39.56 ± 2.01	14.16 ± 1.32	15.52 ± 0.62
	2.76 ± 0.12	49.24 ± 1.51	12.65 ± 0.53	16.98 ± 0.65
	1.63 ± 0.17	58.58 ± 4.09	11.02 ± 1.11	22.81 ± 0.89
	0.69 ± 0.16	66.09 ± 1.85	9.34 ± 0.27	30.94 ± 1.13

Table IV. Estimating and comparing critical instability amplitude.

Author	Method	ξ_{crit}
Miles [27]	Analytical (1D)	$4Y/\sqrt{3}\rho a$
Drucker [30, 31]	Analytical (2D)	$2Y/\rho a$
Dimonte [37]	Experimental (2D)	$Y/\rho a$
Current Work	Experimental (3D)	$1.79 \pm 0.07 Y/\rho a$
	Experimental (2D)	$1.37 \pm 0.06 Y/\rho a$

Table V. Instability tests – varying the perturbation wavelength.

2D/3D	Wavelength - λ (mm)	Initial Amplitude - ξ_i (mm)	Instability Acceleration - a_o (m/s ²)	Instability Amplitude - ξ_o (mm)	Growth Rate - γ (s ⁻¹)
3D	60	3.95 ± 0.17	48.55 ± 1.71	16.13 ± 0.78	13.32 ± 1.21
	30	3.83 ± 0.17	62.66 ± 2.19	15.56 ± 0.85	15.79 ± 0.71
	15	3.87 ± 0.18	70.77 ± 3.33	13.48 ± 1.81	26.83 ± 1.12
2D	60	3.55 ± 0.18	39.56 ± 2.01	14.16 ± 1.32	15.52 ± 0.62
	30	3.52 ± 0.17	49.27 ± 1.60	13.83 ± 0.64	21.16 ± 0.89
	15	3.48 ± 0.17	52.63 ± 2.21	11.38 ± 0.47	27.46 ± 1.03

Table VI. Comparison of Growth Rate Models – varying the perturbation amplitude ($\lambda = 60$ mm).

2D/3D	Wavelength - λ (mm)	Initial Amplitude - ξ_i (mm)	Measured Growth Rate - γ (s^{-1})	Viscous Growth Rate - γ_μ (s^{-1})	Viscous Growth Rate - γ_ν (s^{-1})
3D	60	5.88 ± 0.13	10.86 ± 0.62	20.71 ± 0.89	12.40 ± 1.13
		3.95 ± 0.17	13.32 ± 1.21	27.57 ± 0.70	21.29 ± 1.45
		2.88 ± 0.13	15.78 ± 0.56	34.10 ± 0.44	31.90 ± 0.89
		1.88 ± 0.17	17.79 ± 2.65	40.28 ± 3.03	42.58 ± 5.93
		0.90 ± 0.16	24.34 ± 0.75	47.81 ± 2.60	56.22 ± 4.55
2D	60	5.76 ± 0.13	11.85 ± 0.57	19.20 ± 0.10	11.87 ± 0.17
		3.55 ± 0.18	15.52 ± 0.62	25.50 ± 0.60	26.07 ± 0.99
		2.76 ± 0.12	16.98 ± 0.65	31.06 ± 0.74	28.45 ± 1.01
		1.63 ± 0.17	22.81 ± 0.89	40.97 ± 1.59	50.67 ± 2.01
		0.69 ± 0.16	30.94 ± 1.13	49.89 ± 1.68	61.94 ± 1.91

Table VII. Comparison of Growth Rate Models – varying the perturbation wavelength.

2D/3D	Wavelength - λ (mm)	Initial Amplitude - ξ_i (mm)	Measured Growth Rate - γ (s^{-1})	Viscous Growth Rate - γ_μ (s^{-1})	Viscous Growth Rate - γ_ν (s^{-1})
3D	60	3.95 ± 0.17	13.32 ± 1.21	27.57 ± 0.70	21.29 ± 1.45
	30	3.83 ± 0.17	15.79 ± 0.71	35.34 ± 1.57	18.25 ± 1.85
	15	3.87 ± 0.18	26.83 ± 1.12	48.16 ± 3.62	20.76 ± 3.93
2D	60	3.55 ± 0.18	15.52 ± 0.62	25.50 ± 0.60	26.07 ± 0.99
	30	3.52 ± 0.17	21.16 ± 0.89	32.38 ± 1.18	24.20 ± 1.76
	15	3.48 ± 0.17	27.46 ± 1.03	38.75 ± 1.31	20.21 ± 1.24

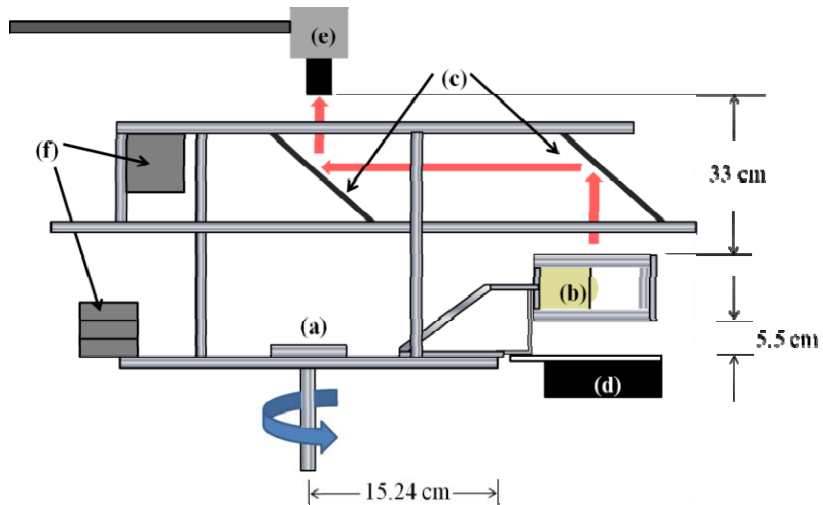


Figure 1. Schematic of RT Strength rotating wheel experiment [Component Labels: (a) rotating disk (b) test section (c) mirror assembly (d) light source (e) high-speed camera (f) counter weights]

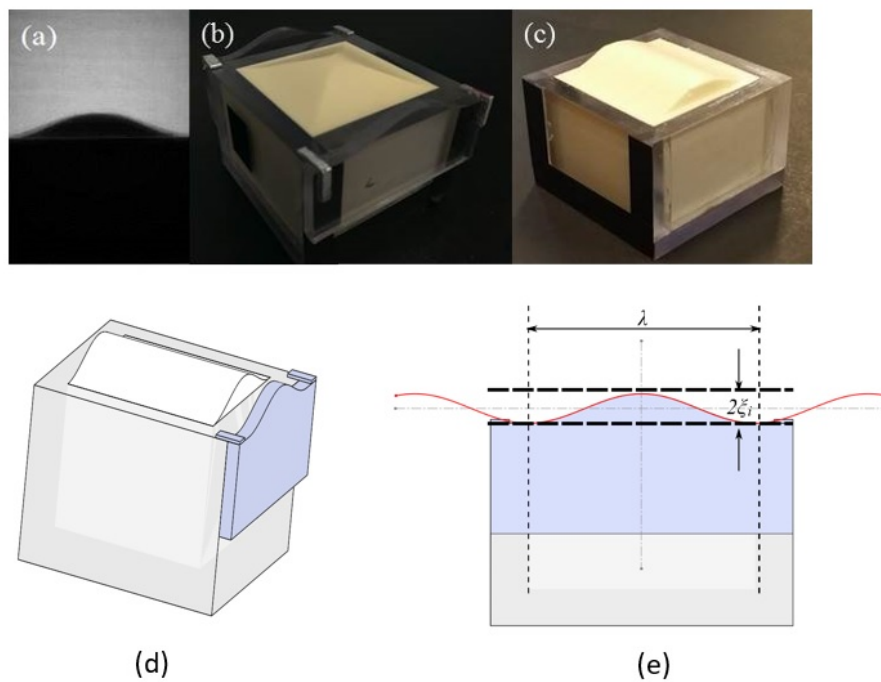


Figure 2. (a) Backlit image of test section at the start of the experiment; (b) initial perturbation 3D interface, $\lambda = 60$ mm $\xi_i = 4$ mm. (c) initial perturbation 2D interface, $\lambda = 60$ mm $\xi_i = 4$ mm. (d) schematics of 3D interface, $\lambda = 60$ mm $\xi_i = 4$ mm, (e) front view of perturbation generated indicating the initial wavelength (λ) and amplitude (ξ_i).

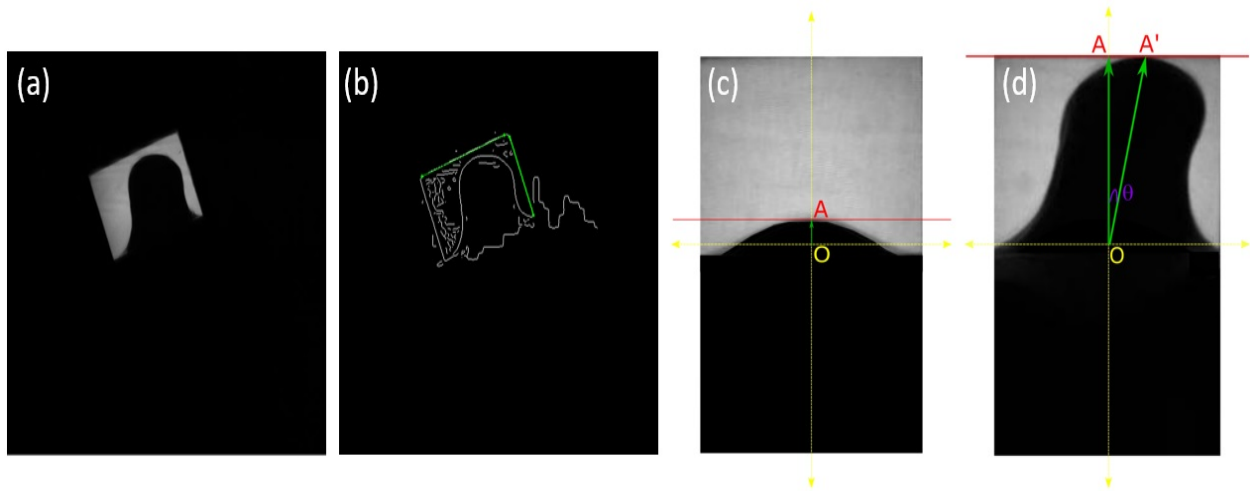


Figure 3. MATLAB image processing of experimental images: (a) original image $\lambda = 60 \text{ mm}$ $\xi_i = 4 \text{ mm}$ 3D interface; (b) edge detection and Hough lines used for rotation; (c) before the perturbation growth where the peak is at the center & (d) near maximum growth where the peak deviates from the normal axis

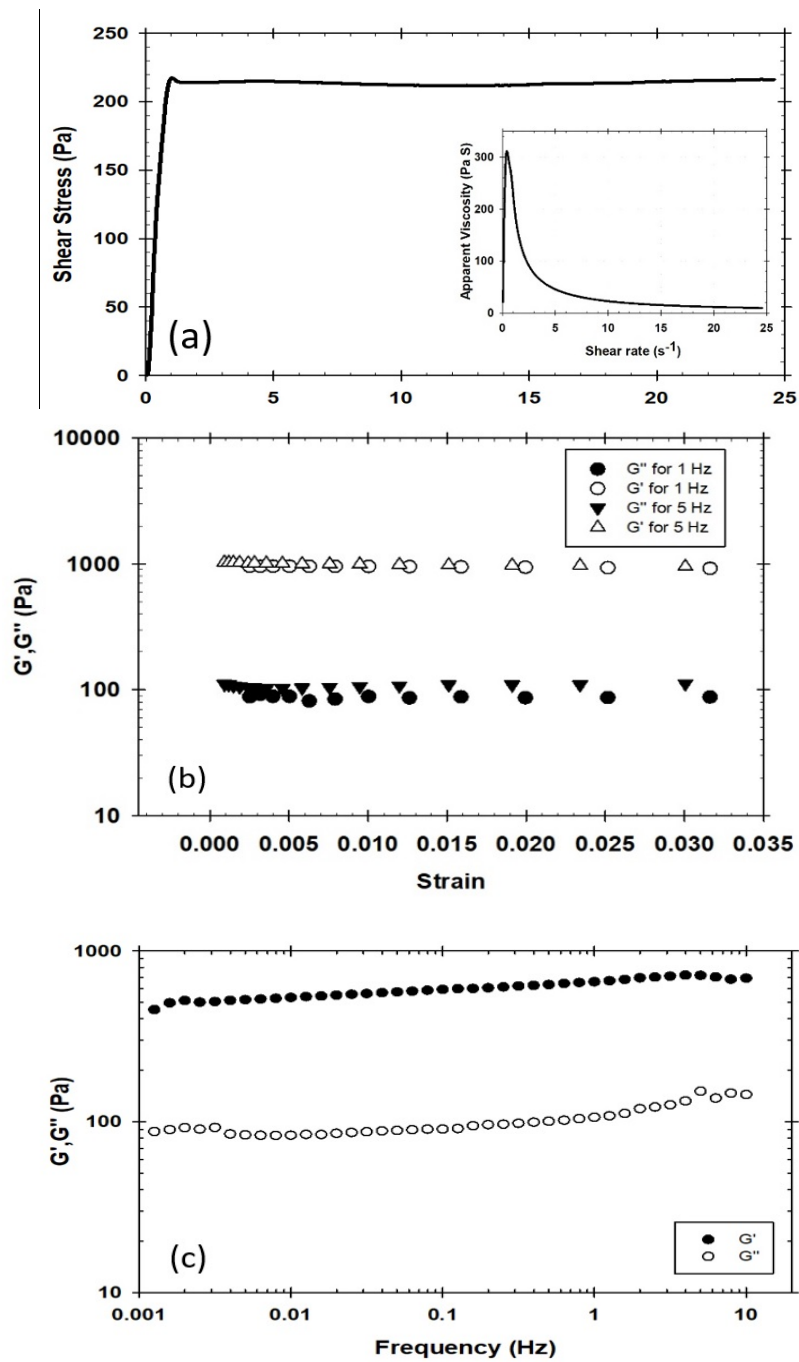


Figure 4. (a) Shear stress and apparent viscosity (inset plot) as a function of shear rate for $\dot{\gamma} = 25 \text{ s}^{-1}$ & $\Delta t = 60 \text{ s}$; (b) storage and viscous moduli vs. strain (amplitude sweep test) for 1 Hz and 5 Hz; (c) storage and viscous moduli vs. amplitude (frequency sweep test) at Strain = 0.1.

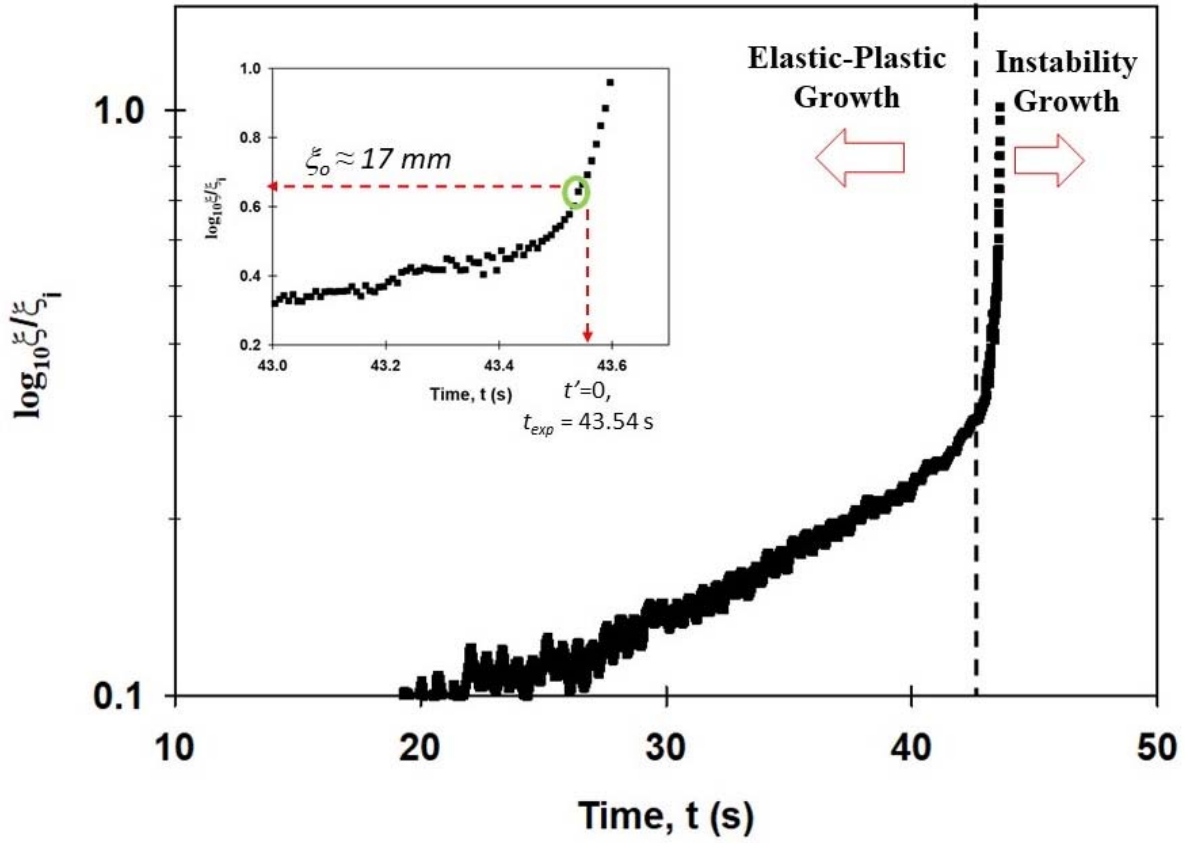


Figure 5. Scaled dimensionless amplitude vs. time plot for the interface with $\xi_i \approx 4\text{mm}$ and $\lambda = 60\text{ mm}$. Regimes of Elastic-Plastic (EP: slow) growth and Instability (IN: fast) growth is observed as the test section is accelerated. The onset of the instability growth is demonstrated in the inset plot defined as $t' = 0$ where $t = 43.54\text{s}$ with the corresponding instability amplitude denoted as ξ_0 .

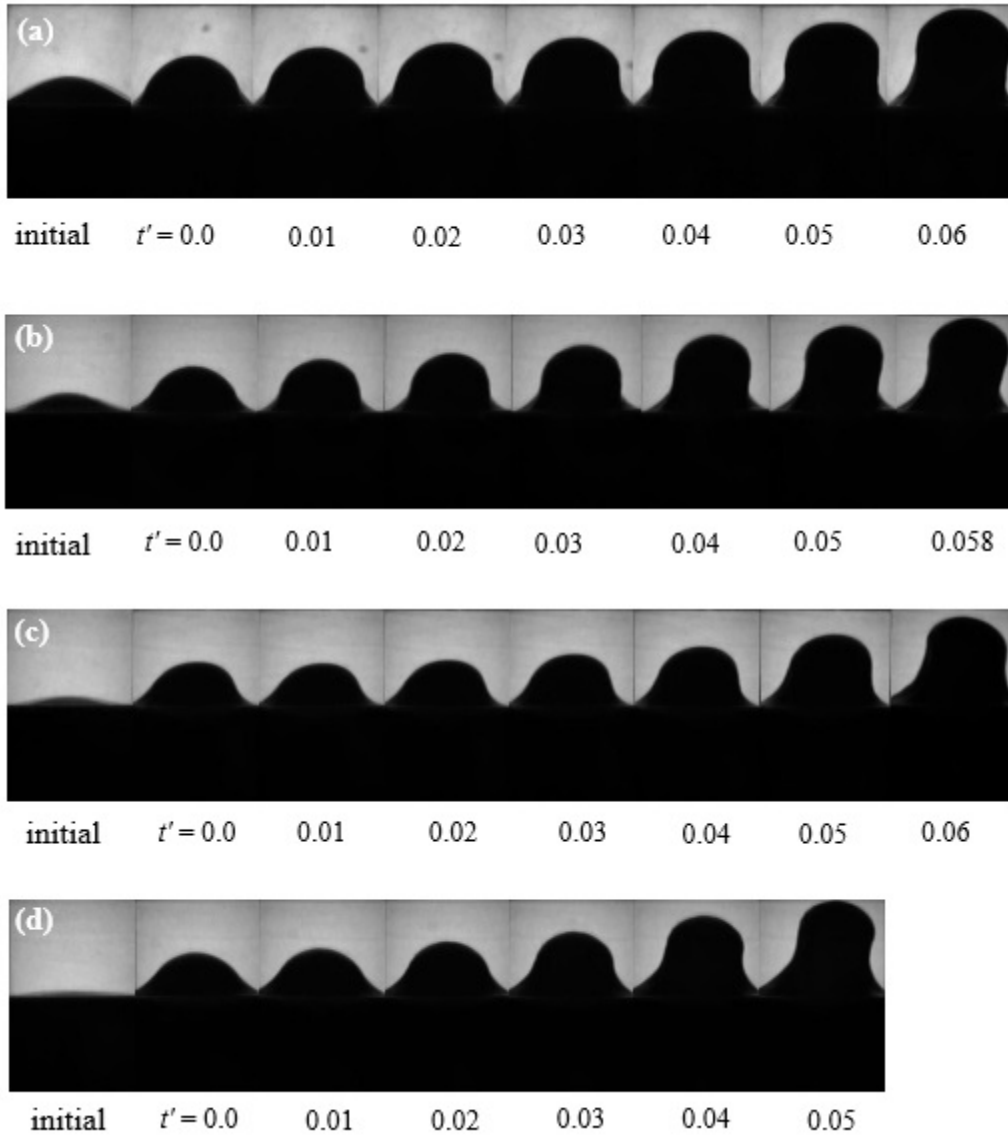


Figure 6. Experimental images for 3D initial perturbation with wavelength (λ) = 60mm and varying initial amplitudes of (a) $\xi_i = 6$ mm (b) $\xi_i = 4$ mm (c) $\xi_i = 2$ mm (d) $\xi_i = 1$ mm, where t' is in seconds.

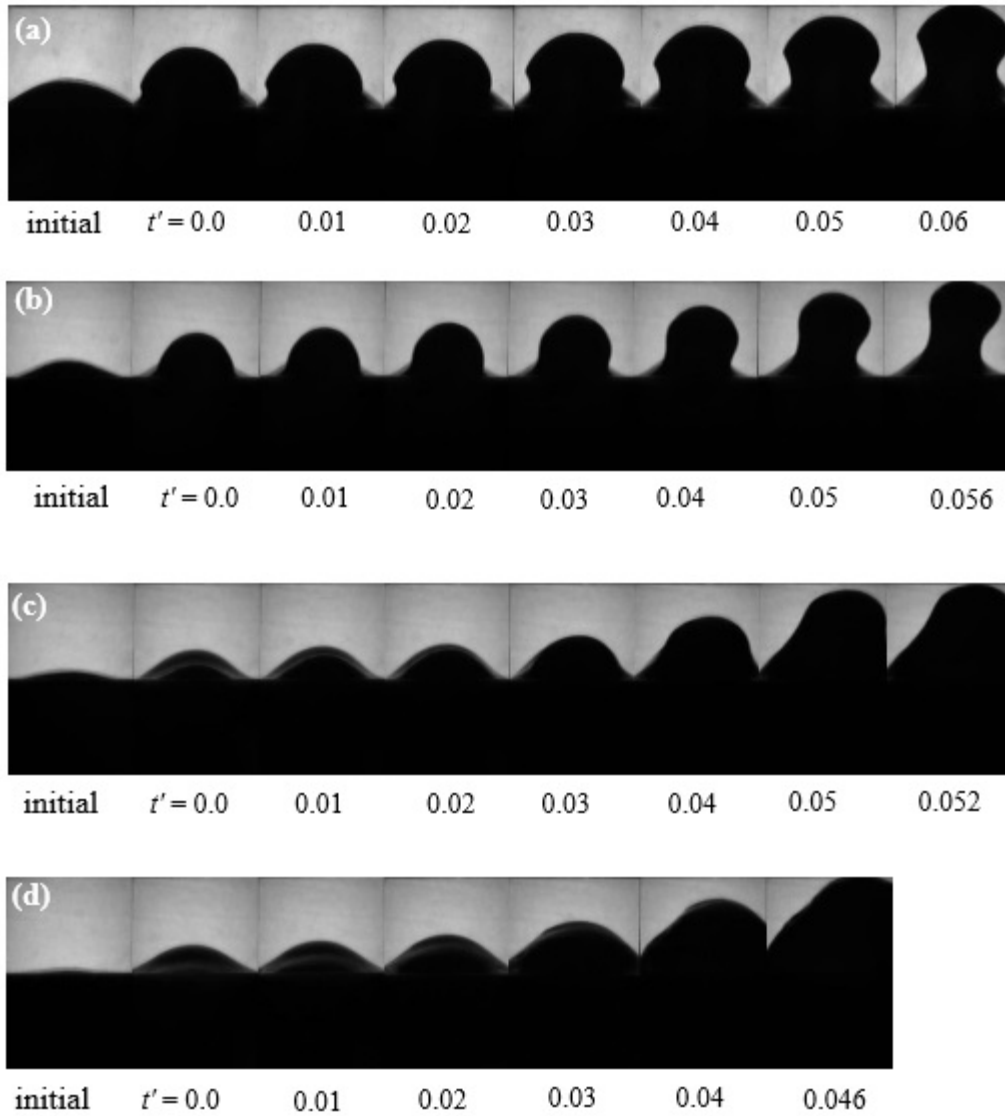


Figure 7. Experimental images for 2D initial perturbation with wavelength (λ) = 60mm and varying initial amplitudes of (a) $\xi_i = 6$ mm (b) $\xi_i = 4$ mm (c) $\xi_i = 2$ mm (d) $\xi_i = 1$ mm, where t' is in seconds.

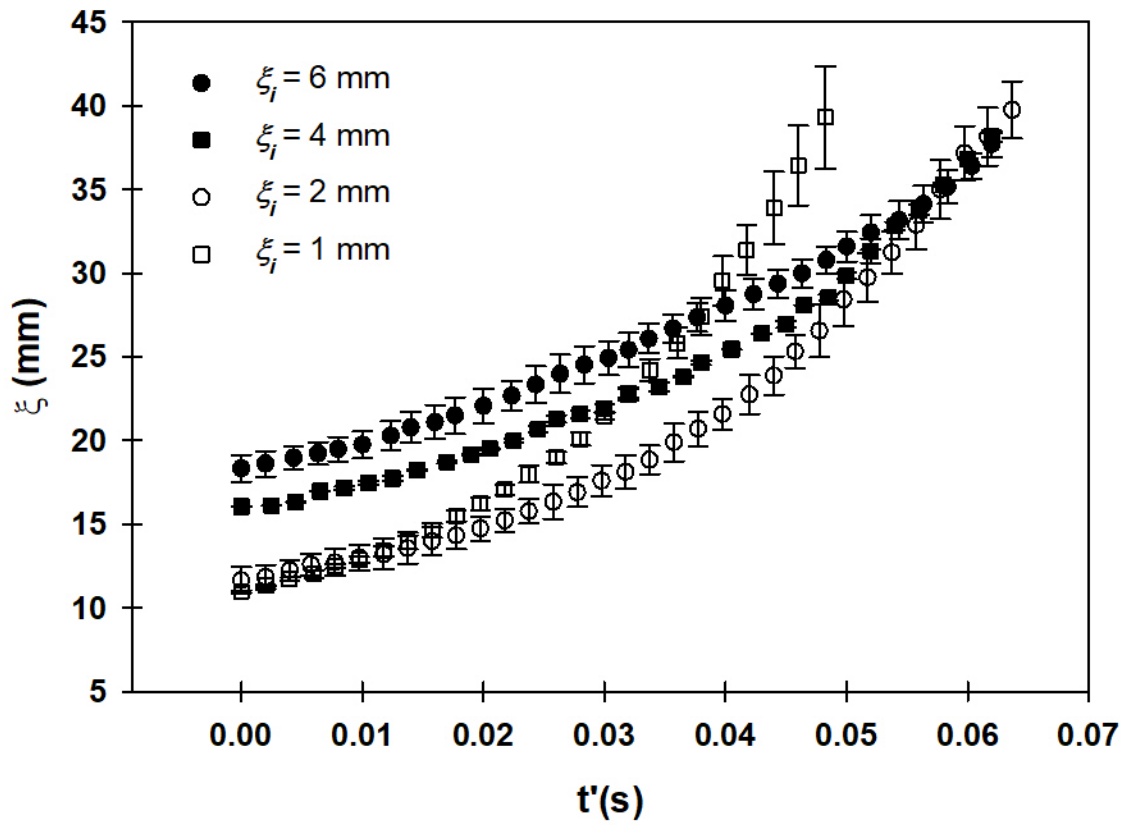


Figure 8. Peak amplitude growth at instability for 3D interface, $\lambda = 60$ mm.

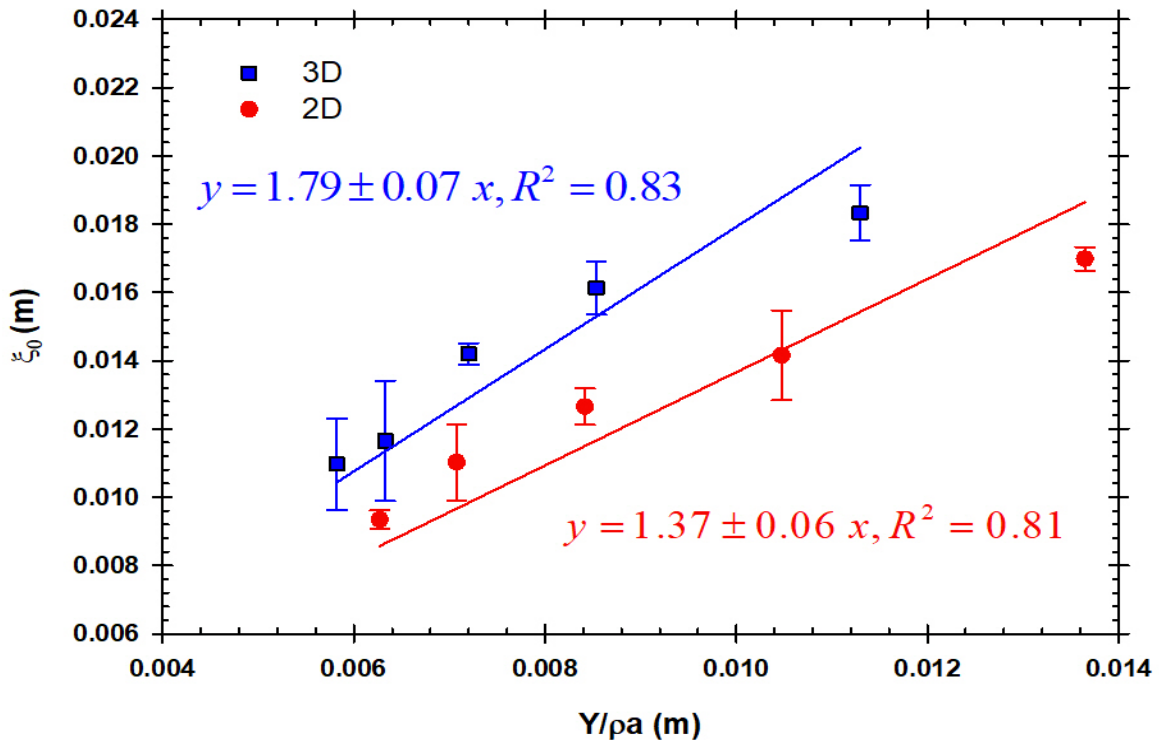


Figure 9. Estimating ξ_{crit} based on the threshold amplitudes (ξ_o) determined from instability tests with varying perturbation amplitude and constant wavelength

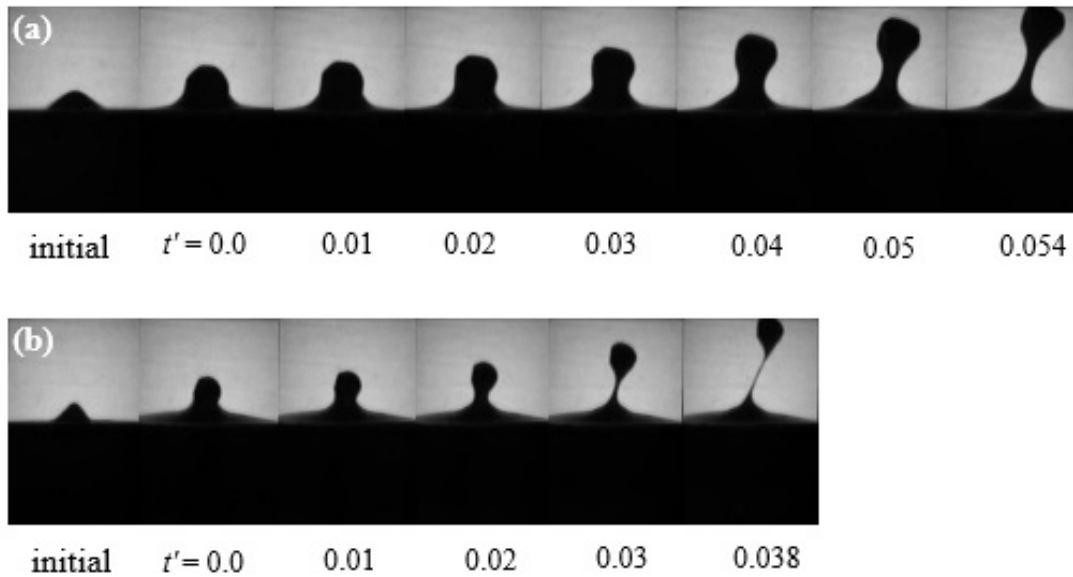


Figure 10. Experimental images for 3D initial perturbation with initial amplitude (ξ_i) = 4 mm and wavelengths: (a) $\lambda = 30$ mm (b) $\lambda = 15$ mm. The time t' is in seconds and is defined at the onset of the instability.

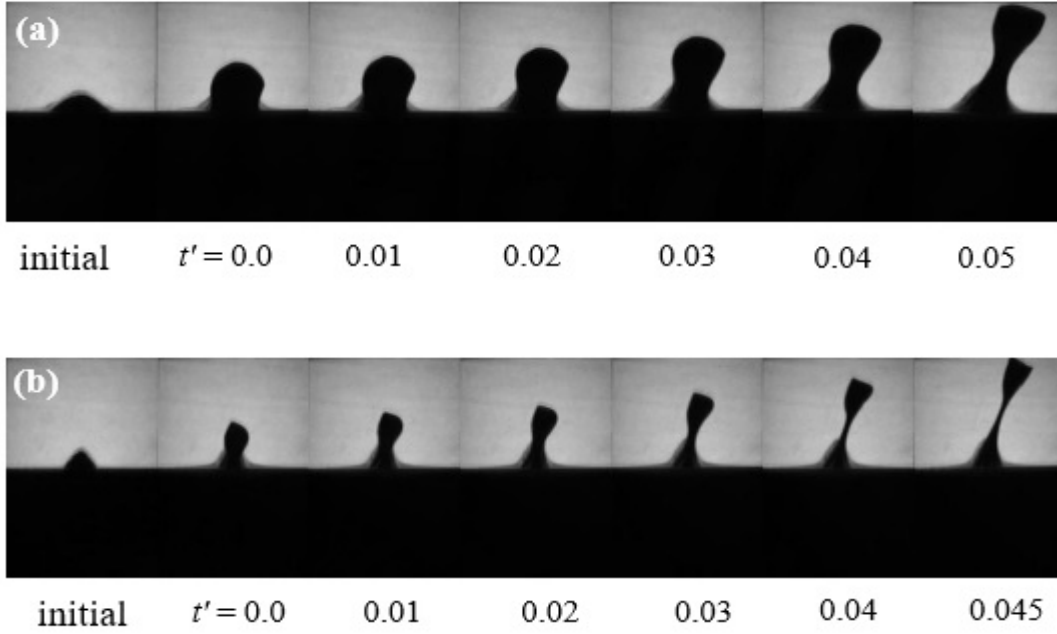


Figure 11. Experimental images for 2D initial perturbation with initial amplitude (ξ_i) = 4 mm and wavelengths: (a) $\lambda = 30$ mm (b) $\lambda = 15$ mm. The time t' is in seconds and is defined at the onset of the instability.

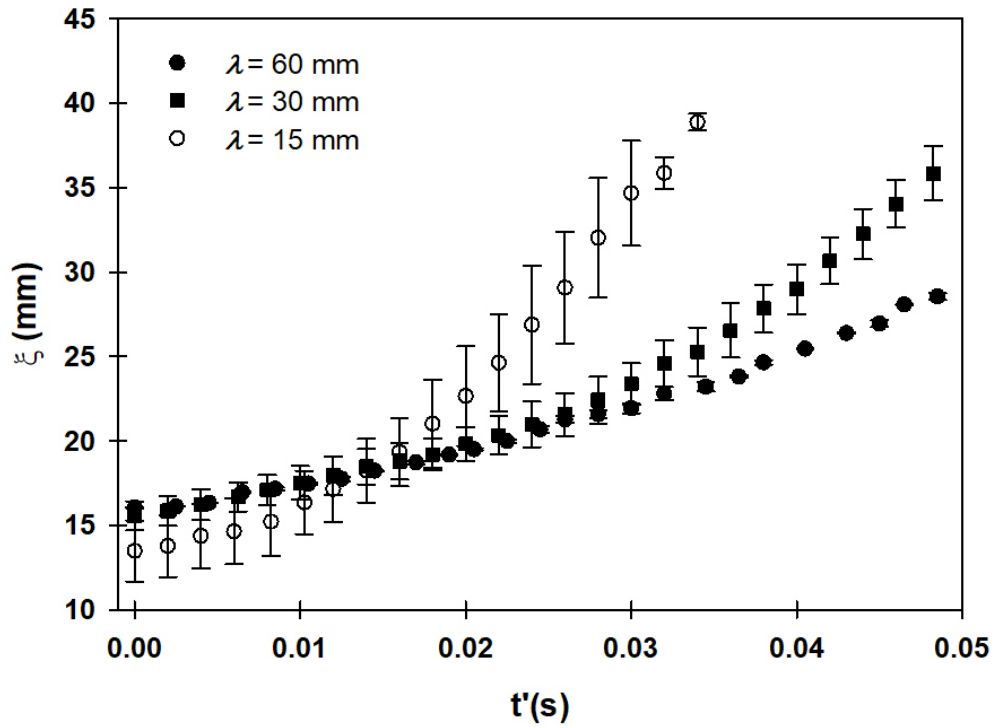


Figure 12. Peak amplitude growth at instability for 3D initial perturbation with $\xi_i = 4$ mm and varying wavelengths.